Optimizing time-of-flight secondary ion mass spectrometry depth profiles of semiconductor heterostructures

Jan Tröger ✉ iD ; Reinhard Kersting iD ; Birgit Hagenhoff iD ; Dominique Bougeard iD ;
Nikolay V. Abrosimov iD ; Jan Klos iD ; Lars R. Schreiber iD ; Hartmut Bracht iD

Check for updates

View Online   Export Citation

Articles You May Be Interested In

Air-stable ambipolar organic thin-film transistors based on an organic homostructure

Appl. Phys. Lett. (June 2005)

DNA-directed assembly of graphene homostructures

J. Appl. Phys. (July 2025)

Liquid-phase-epitaxy homostructure $Pb_{0.85}Sn_{0.15}Te$ diode laser with controlled carrier concentration

Appl. Phys. Lett. (July 1980)

AIP Publishing

Optimizing time-of-flight secondary ion mass spectrometry depth profiles of semiconductor heterostructures

Jan Tröger,[1,2,a] Reinhard Kersting,[2] Birgit Hagenhoff,[2] Dominique Bougeard,[3] Nikolay V. Abrosimov,[4] Jan Klos,[5] Lars R. Schreiber,[5,6] and Hartmut Bracht[1]

AFFILIATIONS

[1]Institute of Materials Physics, University of Münster, 48149 Münster, Germany
[2]Tascon GmbH, 48149 Münster, Germany
[3]Institut für Experimentelle und Angewandte Physik, Universität Regensburg, 93040 Regensburg, Germany
[4]Leibniz-Institut für Kristallzüchtung (IKZ), 12489 Berlin, Germany
[5]JARA-FIT Institute for Quantum Information, Forschungszentrum Jülich GmbH and RWTH Aachen University,
52056 Aachen, Germany
[6]ARQUE Systems GmbH, 52074 Aachen, Germany

[a]Author to whom correspondence should be addressed: jan.troeger@uni-muenster.de

ABSTRACT

The continuous technological development of electronic devices and the introduction of new materials lead to ever greater demands on the fabrication of semiconductor heterostructures and their characterization. This work focuses on optimizing Time-of-Flight Secondary Ion Mass Spectrometry (ToF-SIMS) depth profiles of semiconductor heterostructures aiming at a minimization of measurement-induced profile broadening. As a model system, a state-of-the-art Molecular Beam Epitaxy (MBE) grown multilayer homostructure consisting of ^{nat}Si/^{28}Si bilayers with only 2 nm in thickness is investigated while varying the most relevant sputter parameters. Atomic concentration-depth profiles are determined and an error function based description model is used to quantify layer thicknesses as well as profile broadening. The optimization process leads to an excellent resolution of the multilayer homostructure. The results of this optimization guide to a ToF-SIMS analysis of another MBE grown heterostructure consisting of a strained and highly purified ^{28}Si layer sandwiched between two Si$_{0.7}$Ge$_{0.3}$ layers. The sandwiched ^{28}Si layer represents a quantum well that has proven to be an excellent host for the implementation of electron-spin qubits.

I. INTRODUCTION

Semiconductor heterostructures, i.e., materials with semiconducting properties brought in direct contact with each other, are essential building blocks of modern electronic and optoelectronic devices. Combined into integrated circuits, they are the basis of almost all current information-processing devices, rendering applications such as solar cells, semiconductor lasers, or light-emitting diodes possible.[1–4] Furthermore, the realization of a quantum computer based on semiconductor heterostructures is also a part of the current research study.[5–16] With this advent of quantum technology

applications and constantly progressing miniaturization, the demands on the precision of heterostructures are increasing.[17–20] The use of laser annealing, for example, is being discussed in order to avoid heating up the active region of the spin qubit devices during fabrication,[21] which leads to diffusional broadening of interfaces.

The technology development as well as fabrication control require proper analytical support. In particular, the determination of the material composition, the layer thickness, and the intermixing between the individual layers are of prime importance, since

they have a decisive effect on the performance[20] and the service life of the devices. Several analytical methods are available for this task. A common technique is Scanning Transmission Electron Microscopy (STEM) imaging in combination with Energy Dispersive X-Ray Analysis (EDX) for the determination of the chemical composition. Based on the information carried by secondary electron contrasts, it offers high lateral resolution in the nanometer range and a sensitivity of about 0.1 %.[22] Another method that can be used for composition analysis is Atom Probe Tomography (APT). Based on field ionization and evaporation of atoms from a needle-shaped specimen, it offers sub-nm resolution in three dimensions and sensitivity in the ppm range.[23] In the case sub-nm resolution in three dimensions is not required, a widely used technique for one-dimensional depth profiling is Secondary Ion Mass Spectrometry (SIMS). Primary ions are used for sputtering the sample, which causes the emission of secondary ions from the sample. Using a Time-of-Flight mass spectrometer for mass analysis of the secondary ions (ToF-SIMS), depth resolutions of about 1 nm and high sensitivities in the ppb range can be achieved.[24] Since no special preparation of the samples is necessary, SIMS is generally suitable for routine analysis of semiconductor heterostructures. The sputter process has already been widely studied[25–27] and various approaches to minimize the sputter-related effects that limit the depth resolution by controlling individual measurement parameters have been presented.[28–31] However, the measurement conditions must be properly chosen for each material system to be studied in order to prevent the profile from broadening due to sputter-related effects such as atomic mixing and roughening of the sample surface. This work focuses on optimizing ToF-SIMS depth profiles of semiconductor heterostructures in favor of depth resolution by combining the most promising approaches. Using a test structure that consists of alternating natural Si and ^{28}Si layers each 2 nm in thickness, the influence of the main parameters is demonstrated and quantified. Then, a ^{28}Si quantum well structure sandwiched between SiGe layers is analyzed by ToF-SIMS utilizing optimized instrumental settings that also consider measurement time without significant loss of depth resolution.

II. EXPERIMENTAL

ToF-SIMS depth profiles were recorded on two different samples grown by means of Molecular Beam Epitaxy (MBE). Sample #1 schematically shown in Fig. 1(a) was used as a test structure to study the influence of various instrumental parameters on profile broadening. It consists of four ^{nat}Si/^{28}Si bilayers that were deposited onto a ^{nat}Si buffer layer on top of a ^{nat}Si (001) substrate wafer. Every single layer of the test structure is nominally 2 nm thick. The sample is well suited for several reasons: First, silicon has been extensively studied and is the most common material for semiconductor heterostructures. On the other hand, by controlling the isotopic composition, a well-defined concentration profile of only a single chemical component is obtained. The latter is particularly advantageous since the same chemical properties of the sample components lead to mainly the same sputtering properties and matrix effects are therefore negligible.
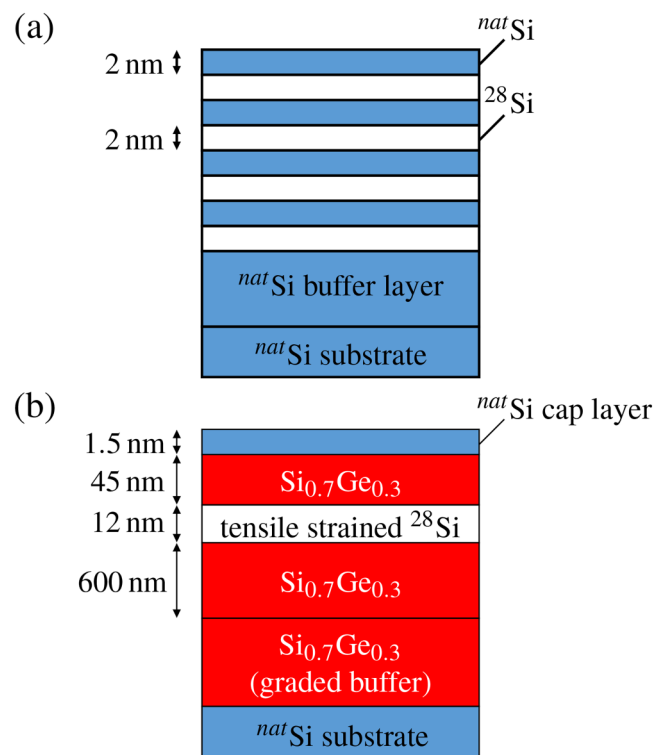
FIG. 1. Schematics of the analyzed samples. (a) Sample #1: a homostructure consisting of four ^{nat}Si/^{28}Si bilayers was deposited onto a ^{nat}Si buffer layer on top of a ^{nat}Si substrate wafer by means of Molecular Beam Epitaxy (MBE). (b) Sample #2: a Si$_{0.7}$Ge$_{0.3}$/^{28}Si/Si$_{0.7}$Ge$_{0.3}$ heterostructure, protected from atmospheric oxygen by a ^{nat}Si cap layer was deposited onto a strain-relaxed graded buffer up to a composition of Si$_{0.7}$Ge$_{0.3}$ on top of a ^{nat}Si substrate wafer. The highly purified and tensile strained ^{28}Si layer represents an electron-spin quantum well.[32]

Sample #2 schematically shown in Fig. 1(b) represents a semiconductor heterostructure that consists of a highly purified and tensile strained ^{28}Si layer sandwiched between two Si$_{0.7}$Ge$_{0.3}$ layers. The upper Si$_{0.7}$Ge$_{0.3}$ layer is protected from oxidation in air by a ^{nat}Si cap layer. The layer stack was deposited onto a strain-relaxed graded buffer up to a composition of Si$_{0.7}$Ge$_{0.3}$ on top of a ^{nat}Si substrate wafer.[20,32] The nominal thicknesses are 1.5 nm for the cap layer, 45 nm for the upper Si$_{0.7}$Ge$_{0.3}$ layer, 12 nm for the ^{28}Si layer, and 600 nm for the lower Si$_{0.7}$Ge$_{0.3}$ layer of constant composition. The growth temperature was 450 °C. In this configuration, the ^{28}Si layer represents a quantum well that is an excellent host for the implementation of electron-spin qubits.[9,14,16,32,33] In both samples, the concentration depth profiles of the host elements were recorded using an IONTOF TOF.SIMS^5 instrument in dual-beam mode.[30,34] For sputtering, a low energy O$_2^+$ ion beam provided by a Dual Source Column (DSC) was used. (The O$_2^+$ ion beam stabilizes the ion yield and makes it independent of oxygen in the residual gas. As it is known that sputtering using O$_2^+$ ion beams can induce additional roughness,[35] the topography of the sputtered area was

analyzed by means of Atomic Force Microscopy.) A small area at the center of the sputter crater was analyzed using a dedicated high energy Bi_x^+ ion beam, provided by a Liquid Metal Ion Gun (LMIG). This approach offers the selection of sputtering and analysis conditions independent of each other.

In a variation study, the instrumental setting was optimized for minimal profile broadening when analyzing structures with only a few monolayers in thickness. Using sample #1, several depth profiles were recorded while varying sputter and analysis parameters. Care was taken to isolate the influence of the individual parameters. However, this was not possible in all cases, as, e.g., the choice of the analysis species, e.g., directly lead to changes in sputter yields. Nevertheless, the data will allow us to get useful guidelines for experimental purposes. All measurements carried out as part of the variation study are summarized in Table I together with the respective conditions. For reference purposes, an instrumental setting used for routine analysis of semiconductor heterostructures with a few nm in thickness was applied first. Sputtering was performed using a O_2^+ ion beam with 500 eV kinetic energy and a current of 81 nA, rastered over an area of $300 \times 300\,\mu m^2$. A Bi_1^+ ion beam with 15 keV kinetic energy and a current of 1.5 pA, was rastered over an area of $100 \times 100\,\mu m^2$ in the center of the sputter crater for analysis. The sample environment was flooded with oxygen gas in a controlled manner to ensure a completely oxidized sample surface throughout the measurement. This primarily avoids sputter-induced roughening that can occur due to different sputter rates of Si and its oxide and shortens the time to reach sputtering equilibrium.[31,37] In addition, the presence of oxygen increases the ionization rate of cations, resulting in higher ion yields and therefore higher sensitivities. Details on the influence of oxygen flooding on the performance in depth profiling were discussed by Ng *et al.*[37] As a reference, the partial pressure of oxygen was set to 2×10^{-6} mbar. Secondary ions of positive polarity were analyzed. These settings, referred to below as standard measuring conditions (SMCs), represent a compromise between mass resolution, lateral resolution, depth resolution, and measurement time. In a series of measurements, the instrumental parameters were optimized in favor of depth resolution. First, the influence of the flood

gas pressure, the primary ion current of the analysis beam, and the primary ion species used for analysis were investigated. Finally, the sputtering conditions were optimized, with the energy of the sputter beam being the essential parameter. Changing one parameter was followed by the acquisition of a new depth profile, respectively, before the parameter was reset and another parameter was addressed. The sputter time was converted into a depth scale by measuring the depth of the sputter crater using an IONTOF Atomic Force Microscope (AFM) based mechanical profilometer, which offers a wide scan range. After calibrating the profilometer using a step height standard (VLSI Standards Inc., model: nSHS-8800C), the crater depth was determined as the arithmetic mean of ten measurements with a standard deviation of about 0.1 nm. The intensities were converted into a concentration scale referring to the isotopic distribution in ^{nat}Si.[38]

Depth profiling of the semiconductor heterostructure (sample #2) was performed using a O_2^+ ion beam with 500 eV kinetic energy and a maximum current of 40 nA for sputtering, rastered over an area of $300 \times 300\,\mu m^2$. A Bi_1^+ ion beam with 15 keV kinetic energy and a current of 1.5 pA was rastered over an area of $75 \times 75\,\mu m^2$ in the center of the sputter crater for analysis. Oxygen gas flooding was used with the partial pressure being 1×10^{-6} mbar. Secondary ions of positive polarity were analyzed. The sputter time was converted into a depth scale by measuring the depth of the sputter crater using an BRUKER DektakXT mechanical profilometer. After calibrating the profilometer using a step height standard (Veeco, model: 138 367), the crater depth was determined as the arithmetic mean of three measurements with a standard deviation of about 2.4 nm. The intensities were converted into a concentration scale considering the isotope distribution in the $Si_{0.7}Ge_{0.3}$ layers, which was determined based on the isotope distributions[38] and the atomic densities[38] of ^{nat}Si and ^{nat}Ge.

The broadening and the layer thickness were determined by fitting a model function that has been widely used for the analysis of self-atom profiles and its broadening in semiconductor heterostructures.[39–43] Every interface was assumed to be described by an error function. Following this approach, the concentration

TABLE I. Overview of all SIMS analysis conditions applied for Si depth profiling of sample #1. SMC: standard measuring conditions, X_j: ion species, E_j: beam energy, I_j: beam current, D_j: ion dose, Y_j: estimated sputter yield[36] at an angle of incidence (45°), A_j: rastered area, T_j: sputter time, p: partial pressure of the flood gas, wherein $j = sp$ represents the sputter beam and $j = an$ the analysis beam. A ↑ symbol indicates an increase and a ↓ symbol indicates a decrease in the respective parameter.

Variation	X_{sp}	E_{sp} (eV)	I_{sp} (nA)	D_{sp} ($\times 10^{14}$)	Y_{sp}	A_{sp} (μm^2)	X_{an}	E_{an} (keV)	I_{an} (pA)	D_{an} ($\times 10^9$)	Y_{an}	A_{an} (μm^2)	T_{sp}/T_{an}	p (mbar)
SMC	O_2^+	500	81.0	5.06	0.65	300×300	Bi_1^+	15	1.5	9.36	4.52	100×100	1:1	2×10^{-6}
$p \uparrow$	O_2^+	500	81.0	5.06	0.65	300×300	Bi_1^+	15	1.5	9.36	4.52	100×100	1:1	4×10^{-6}
$p \downarrow$	O_2^+	500	81.0	5.06	0.65	300×300	Bi_1^+	15	1.5	9.36	4.52	100×100	1:1	5×10^{-7}
$I_{an} \uparrow$	O_2^+	500	81.0	5.06	0.65	300×300	Bi_1^+	15	12.8	79.9	4.52	100×100	1:1	2×10^{-6}
$I_{an} \downarrow$	O_2^+	500	81.0	5.06	0.65	300×300	Bi_1^+	15	0.2	1.25	4.52	100×100	1:1	2×10^{-6}
X_{an}	O_2^+	500	81.0	5.06	0.65	300×300	Bi_3^+	15	0.9	5.62	8.22[a]	100×100	1:1	2×10^{-6}
$E_{sp} \downarrow$	O_2^+	250	20.0	11.2	0.32	300×300	Bi_1^+	15	1.5	84.4	4.52	100×100	1:1	2×10^{-6}
Optimized	O_2^+	250	16.2	12.1	0.32	300×300	Bi_1^+	13	1.5	4.61	4.26	75×75	24:1	2×10^{-6}

[a]There is no literature reference on the sputter yield of Bi_3^+. Assuming that the three cluster atoms impact individually and thus ignoring any non-linear or cooperative effects, we estimated the sputter yield by using thrice the value of 5 keV Bi_1^+.

23 December 2025 12:56:36

profiles C^* (^{28}Si, ^{29}Si, ^{30}Si) of sample #1 are described by

$$C^* = \frac{C_1 + C_3}{2} + \frac{C_1 - C_2}{2} \sum_{i=1}^{7} (-1)^i \text{erf}\left(\frac{z - z_i}{r_i}\right) + \frac{C_3 - C_2}{2} \text{erf}\left(\frac{z - z_8}{r_8}\right), \quad (1)$$

where C_1 is the concentration of a Si isotope in the ^{nat}Si layers, C_2 is the concentration in the isotopically purified ^{28}Si layers, C_3 is the concentration in the ^{nat}Si buffer layer, r_i describes the broadening of interface i, counted starting at the sample surface, and z_i with $z_{i+j} = z_i + z_{i+1} + \cdots + z_{i+j-1}$ stands for the layer thickness. Fitting was done by applying the least square method, using r_i, z_i and C_2 as free parameters. The concentration profiles C^* (^{28}Si, ^{29}Si, ^{30}Si, ^{70}Ge, ^{72}Ge, ^{73}Ge, ^{74}Ge, ^{76}Ge) of sample #2 are described by

$$C^* = \frac{C_1 + C_3}{2} - \frac{C_1 - C_2}{2} \text{erf}\left(\frac{z - z_1}{r_1}\right) + \frac{C_3 - C_2}{2} \text{erf}\left(\frac{z - z_2}{r_2}\right), \quad (2)$$

where C_1 is the concentration of a Si or Ge isotope in the upper Si$_{0.7}$Ge$_{0.3}$ layer, C_2 is the concentration in the isotopically purified ^{28}Si quantum well, C_3 is the concentration in the lower Si$_{0.7}$Ge$_{0.3}$ layer, r_i describes the broadening of interface i, counted starting at the sample surface, and z_i with $z_{i+j} = z_i + z_{i+1} + \cdots + z_{i+j-1}$ stands for the layer thickness, respectively. Fitting was done applying the least square method, using r_i, z_i, and C_2 as free parameters.

A Park Systems XE-100 Atomic Force Microscope (AFM) was used for topography analysis on both samples (#1 and #2). Using a NSC15 tip, an area of $8 \times 8\,\mu\text{m}^2$ was scanned in non-contact mode. AFM analysis was performed on the sample surface and in the crater resulting from the ToF-SIMS measurements.

III. RESULTS AND DISCUSSION

### A. Depth profiling of a test homostructure—A parameter variation study

The results of the measurement using standard measuring conditions are shown in Fig. 2. Profiles of all three stable Si isotopes are shown. The measured ^{29}Si and ^{30}Si intensities show a clearly visible modulation. A similar modulation is observed for the measured ^{28}Si intensity, but with smaller differences between local minima and maxima of the measured intensity compared to the ^{29}Si and ^{30}Si signals that are not visible on the logarithmic scale. The reason is smaller differences in the ^{28}Si concentration between the ^{nat}Si layers and the purified ^{28}Si layers in comparison to the ^{29}Si concentration and the ^{30}Si concentration resulting directly from the isotopic distribution of ^{nat}Si. For the parameter variation study, the ^{30}Si signal was selected because it is less affected by interference with hydrates compared to the ^{29}Si signal, especially in the near-surface region. As shown in Fig. 3, the ^{29}Si peak is observed in overlap with a ^{28}SiH peak (a), while the ^{30}Si peak (b) appears much steeper. The interference of ^{29}Si and ^{28}SiH leads to an overestimation of the ^{29}Si concentration within the first few nm in Fig. 2, which is not observed for ^{30}Si.
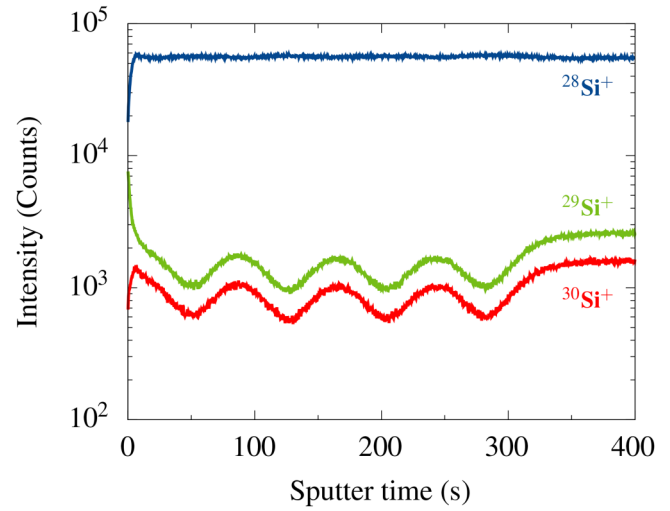
FIG. 2. SIMS depth profiles of ^{28}Si, ^{29}Si, and ^{30}Si in the four-bilayer ^{nat}Si/^{28}Si test structure. Measurement conditions: O$_2^+$, 500 eV, 81 nA, $300 \times 300\,\mu\text{m}^2$ sputtering; Bi$_1^+$, 15 keV, 1.5 pA, $100 \times 100\,\mu\text{m}^2$ analysis; O$_2$, 2×10^{-6} mbar flooding.

1. Influence of the flood gas pressure

Using oxygen gas flooding with a partial pressure of 2×10^{-6} mbar, the ^{30}Si signal was detected with maximum intensity. When the partial pressure was increased to 4×10^{-6} mbar, no significant influence on the measured profile was observed. In
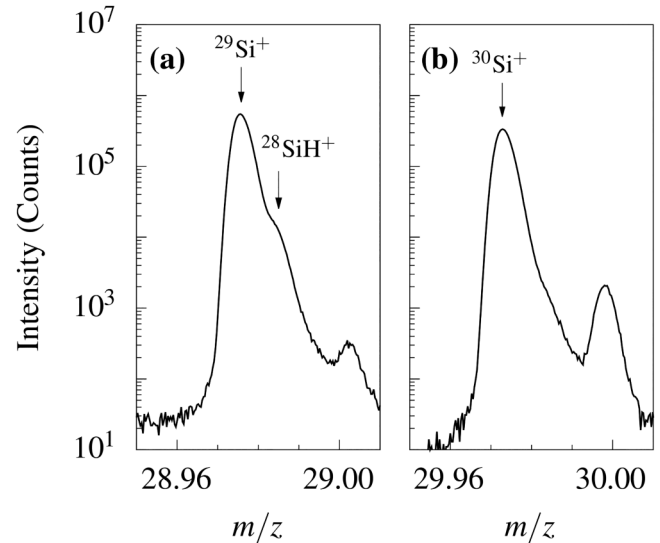
FIG. 3. Sections of the mass spectrum of the test structure. On the right side of the ^{29}Si peak, an interference with ^{28}SiH is observed (a), while the right side of the ^{30}Si peak (b) appears much steeper.

23 December 2025 12:56:36

contrast, a reduction in the partial oxygen pressure leads to a clearly stronger profile broadening (not shown as a figure) followed by an increase in secondary ion intensity during the first few nm. This suggests an increasing concentration of ^{30}Si within the uppermost ^{nat}Si layer. This is related to the reaction rate of the oxidation process.[37] Below a partial pressure of 2×10^{-6} mbar, the maximum reaction rate for the oxidation of the sample surface is not reached and implantation of oxygen into the sample surface during the sputter process leads to an increasing ion intensity, until the sputter equilibrium is reached, thereby suggesting an increased concentration of ^{30}Si. A partial pressure of 2×10^{-6} mbar is considered to be sufficient to establish equilibrium conditions after short sputter times and accordingly was kept for the following measurements.

### 2. Influence of the analysis beam current

The ion current of the analysis beam has a noticeable influence on the profile: increasing the ion current leads to higher intensities but lower dynamic range and visible profile broadening, which increases with depth as shown in Fig. 4(a). These effects are caused by the larger number of high-energy ion collisions, resulting in strong atomic mixing and damage of the sample structure that accumulates with depth. (Further explanations considering the sputter rate ratio are given in Sec. III A 4.) In contrast, decreasing the ion current extends the dynamic range and lowers the profile broadening, but also leads to stronger scattering of the data, as shown in Fig. 4(b). The statistical uncertainty of the data scales with $\sqrt{N}/N$ where N describes the measured ion intensity (counts). Reducing the primary ion current directly leads to lower secondary ion intensities, resulting in lower accuracy of the data. Therefore, decreasing the primary ion current does not improve the profile quality any further, compared to the SMC profile.

3. Influence of the analysis beam species

Theoretically, the use of Bi_3^+ instead of Bi_1^+ should be advantageous for depth resolution. Bi_3^+ is a cluster ion that dissociates when it hits the sample surface, whereby each of the individual Bi atoms deposits only a fraction of the total beam energy near the point of impact. This leads to a broader distribution of total energy and should confine the bombardment-induced atomic mixing to a smaller volume. The extent of this confinement has been discussed in the SIMS community for many years.[44] However, the energy distribution during ion impact is a complex process and the actual energy deposition can vary significantly depending on the ion surface interaction dynamics. Under the specific working conditions in this study, the use of Bi_3^+ clusters showed no visible effect in improving the depth resolution compared to Bi_1^+, as shown in Fig. 5.

### 4. Influence of the sputter beam energy

It is well known that the energy of sputtering ions is crucial for depth resolution in sputter depth profiling and effects that lead to profile broadening general scale with the sputtering energy. Therefore, reducing the sputtering energy is obvious while optimizing the analysis conditions for minimal profile broadening. In Fig. 6(a), a profile acquired reducing the sputtering energy from
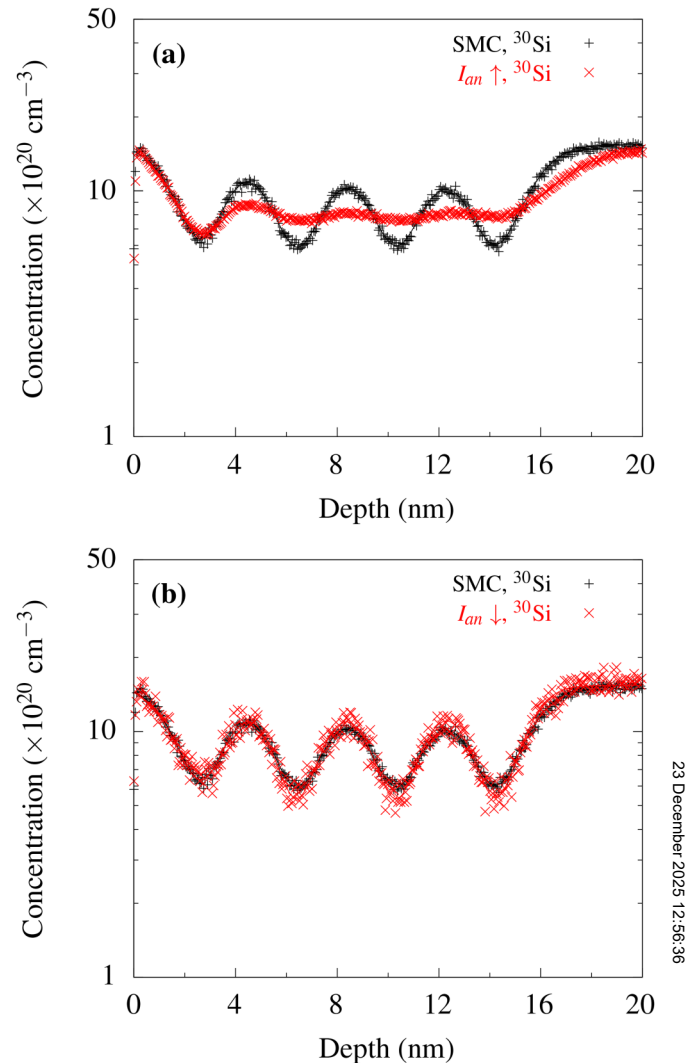
FIG. 4. SIMS concentration-depth profiles of ^{30}Si in the four-bilayer $^{nat}Si/^{28}Si$ test structure, recorded under different experimental conditions. Plus signs mark data points recorded under standard measuring conditions (O_2^+, 500 eV, 81 nA, $300 \times 300 \, \mu m^2$ sputtering; Bi_1^+, 15 keV, 1.5 pA, $100 \times 100 \, \mu m^2$ analysis; O_2, 2×10^{-6} mbar flooding). Crosses mark data points recorded with the analysis beam current increased to 12.8 pA (a) and decreased to 0.2 pA (b), respectively. Every third data point is shown for clarity. The solid lines represent the best fits based on Eq. (1) taking sputter broadening effects into account. The relative statistical uncertainties $\sqrt{N}/N$, where N describes the measured ion intensity (counts), vary between 0.02 and 0.04 (SMC), 0.008 and 0.011 ($I_{an} \uparrow$), and 0.06 and 0.12 ($I_{an} \downarrow$), respectively.

500 to 250 eV is shown in comparison to the SMC profile. Instead of an improvement in profile quality, a lack of dynamic range and strong profile broadening that increases with depth is observed. The profile shows some similarities to the profile acquired after increasing the primary ion current [Fig. 4(a)] suggesting a similar reason, i.e., structural damage caused by the high-energy analysis
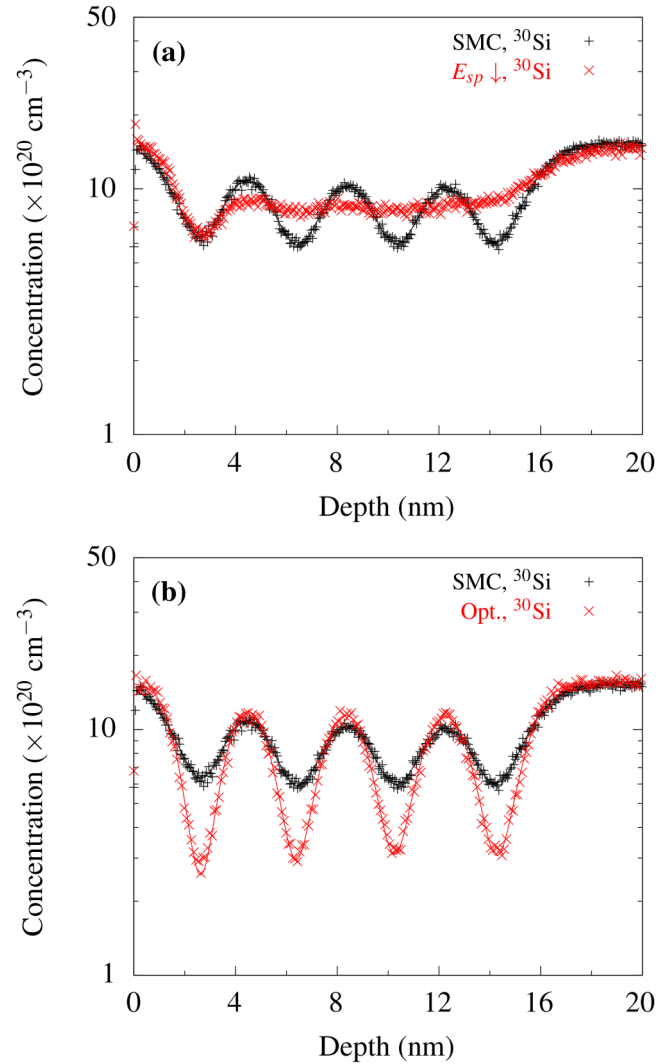
23 December 2025 12:56:36
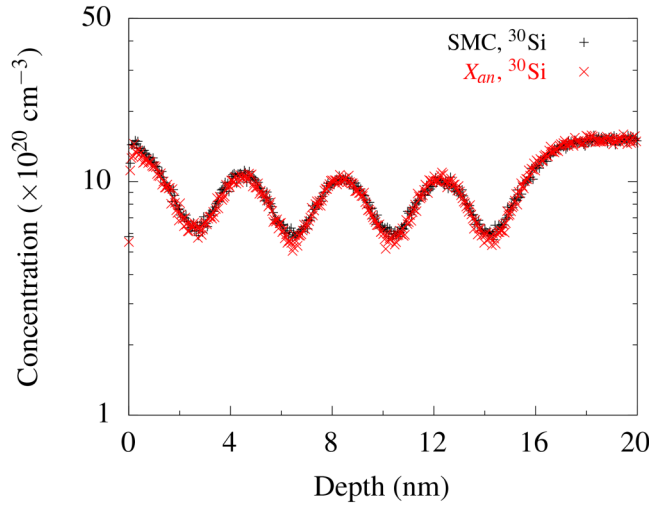
FIG. 5. SIMS concentration-depth profiles of ^{30}Si in the four-bilayer ^{nat}Si/^{28}Si test structure, recorded under different experimental conditions. Plus signs mark data points recorded under standard measuring conditions (O$_2^+$, 500 eV, 81 nA, $300 \times 300\,\mu$m^2 sputtering; Bi$_1^+$, 15 keV, 1.5 pA, $100 \times 100\,\mu$m^2 analysis; O$_2$, 2×10^{-6} mbar flooding). Crosses mark data points recorded using a Bi$_3^+$ cluster ion beam with a current of 0.9 pA for analysis compared to the reference conditions. Every third data point is shown for clarity. The solid lines represent the best fits based on Eq. (1) taking sputter broadening effects into account. The relative statistical uncertainties $\sqrt{N}/N$, where N describes the measured ion intensity (counts), vary between 0.02 and 0.04 (SMC) and 0.03 and 0.04 (X_{an}), respectively.

beam. While increasing the ion current enhances collision-induced atomic mixing, reducing the sputtering energy primarily affects (lowers) the ion penetration depth and surface atom mobility, which leads to significantly slower material removal. However, if all other parameters, in particular, the number of analysis cycles between two sputtering cycles is kept constant, the high-energy analysis beam hits the sample much more often before the profile has been fully recorded. Note that the number of data points in the profile $E_{sp} \downarrow$ is significantly higher compared to the SMC profile [Fig. 6(a)]. The higher dose of high-energy primary ions leads to the observed structural damage. This shows while reducing the sputtering energy, the contribution of the analysis beam to the material removal has to be taken into account. The amount of material removed by both, the sputter and analysis beam, is described by the sputter rate ratio R^*. It is defined by

$$R^* = \frac{R_{sp}}{R_{an}} \propto \frac{D_{sp}}{D_{an}} \cdot \frac{Y_{sp}}{Y_{an}} \cdot \frac{A_{an}}{A_{sp}}, \quad (3)$$

where D_j is the ion dose, Y_j is the yield, and A_j is the rastered area of the sputter beam ($j = sp$) and the analysis beam ($j = an$), respectively.[30,45] According to experimental data,[45] a limit value for significant loss of depth resolution is $R^* \approx 500$, while an improvement of depth resolution with increasing R^* is observed up to $R^* \approx 1000$. Below the lower limit, the material removal is no longer

FIG. 6. SIMS concentration-depth profiles of ^{30}Si in the four-bilayer ^{nat}Si/^{28}Si test structure, recorded under different experimental conditions. Plus signs mark data points recorded under standard measuring conditions (O$_2^+$, 500 eV, 81 nA, $300 \times 300\,\mu$m^2 sputtering; Bi$_1^+$, 15 keV, 1.5 pA, $100 \times 100\,\mu$m^2 analysis; O$_2$, 2×10^{-6} mbar flooding). Crosses mark data points recorded with a sputter beam energy decreased to 250 eV reaching a maximum beam current of 20 nA. (a) The sputter rate ratio was not taken into account and were calculated to be 104. Every third (SMC) and every 40th ($E_{sp} \downarrow$) data point is shown for clarity. (b) The sputter rate ratio was taken into account (Bi$_1^+$, 13 keV, $75 \times 75\,\mu$m^2 analysis; sputter time between consecutive analysis cycles extended) and calculated to be 1233. Every third data point is shown for clarity. The solid lines represent best fits based on Eq. (1) taking sputter broadening effects into account. The relative statistical uncertainties $\sqrt{N}/N$, where N describes the measured ion intensity (counts), vary between 0.02 and 0.04 (SMC and $E_{sp} \downarrow$) and 0.03 and 0.06 (Opt.), respectively.

dominated by the sputter beam and structural damage caused by the analysis beam can accumulate during the measurement.

For the profile $E_{sp} \downarrow$ in Fig. 6(a), the sputter rate ratio R^* was calculated to be 104, which is well below the limit for significant

23 December 2025 12:56:36

loss of depth resolution. In order to successfully perform depth profiling with low energies, the sputter rate ratio must be brought to the upper limit, i.e., it must be ensured that the material removal of the sputter beam is high enough to ignore the influence of the analysis beam. Therefore, the sputtering time between successive analysis cycles was significantly increased by a factor of 24 affecting the sputter rate ratio positively. The effect was expected to be high enough so that the analysis area could be decreased to $75 \times 75\,\mu m^2$, which generally affects the sputter rate ratio negatively. Additionally, the analysis beam energy was reduced to 13 keV affecting the sputter rate ratio positively due to a lower ion yields Y_{an} and might reduce atomic mixing during analysis. However, the effect will be small as the energy was only changed by 13 %. Overall, the resulting sputter rate ratio was calculated to 1233, which is well above the upper limit. In the profile shown in Fig. 6(b), a larger dynamic range and significantly reduced instrumental broadening is observed.

For comparison, the sputter rate ratios were calculated for all recorded profiles and summarized in Table II. In case of $I_{an} \uparrow$ and $E_{sp} \downarrow$, the limit of $R^\star \approx 500$ was not reached. All further measurements revealed a sputter rate ratio of $R^\star > 500$. For the SMC profile, as well as the profiles $p \downarrow$, $p \uparrow$, and X_{an} the respective sputter rate ratios of 864 and 791 are well above the lower limit of $R^\star \approx 500$, but still below $R^\star \approx 1000$ indicating room for optimization. The highest sputter rate ratio of 6468 was determined for the profile $I_{an} \downarrow$, but the profile $E_{sp}^\star \downarrow$ that revealed a sputter rate ratio of 1232 shows higher depth resolution [cf. Figs. 4(b) and 6(b)]. This confirms that the sputtering rate ratio determines the depth resolution only up to $R^\star \approx 1000$ and beyond the sputtering energy is dominant.

5. Evaluation of the fit results

The results for the fit parameters r_i that describe the interfacial broadening of sample #1 are graphically shown in Fig. 7. The

TABLE II. Sputter rate ratios $R^\star$ and average changes in the interfacial broadening $\varnothing r_i$ compared to the standard measuring conditions (SMCs) profile. Positive values indicate an increase, while negative values indicate an improvement in interfacial broadening. p: partial pressure of the flood gas, I_j: beam current, X_j: ion species, E_j: beam energy, wherein $j = sp$ represents the sputter beam and $j = an$ the analysis beam. A ↑ symbol indicates an increase and a ↓ symbol indicates a decrease in the respective parameter. n.d.: value not determined.

Variation	Figure	$R^\star$	$\varnothing r_i$ (%) $i=1,3,5,7$	$\varnothing r_i$ (%) $i=2,4,6,8$	$\varnothing r_i$ (%) $i=1,\dots,8$
SMC	4–6	864	0	0	0
$p \uparrow$	…	864	−9	+3	−3
$p \downarrow$	…	864	+33	−9	+12
$I_{an} \uparrow$	4(a)	101	n.d.	n.d.	n.d.
$I_{an} \downarrow$	4(b)	6468	−6	−9	−8
X_{an}	5	791[a]	−2	−2	−2
$E_{sp} \downarrow$	6(a)	104	n.d.	n.d.	n.d.
Optimized	6(b)	1232	−28	−26	−27

[a]Note that the given sputter rate ratio is a rough estimate since the sputter yield of Bi_3^+ is not exactly known (see Table I).
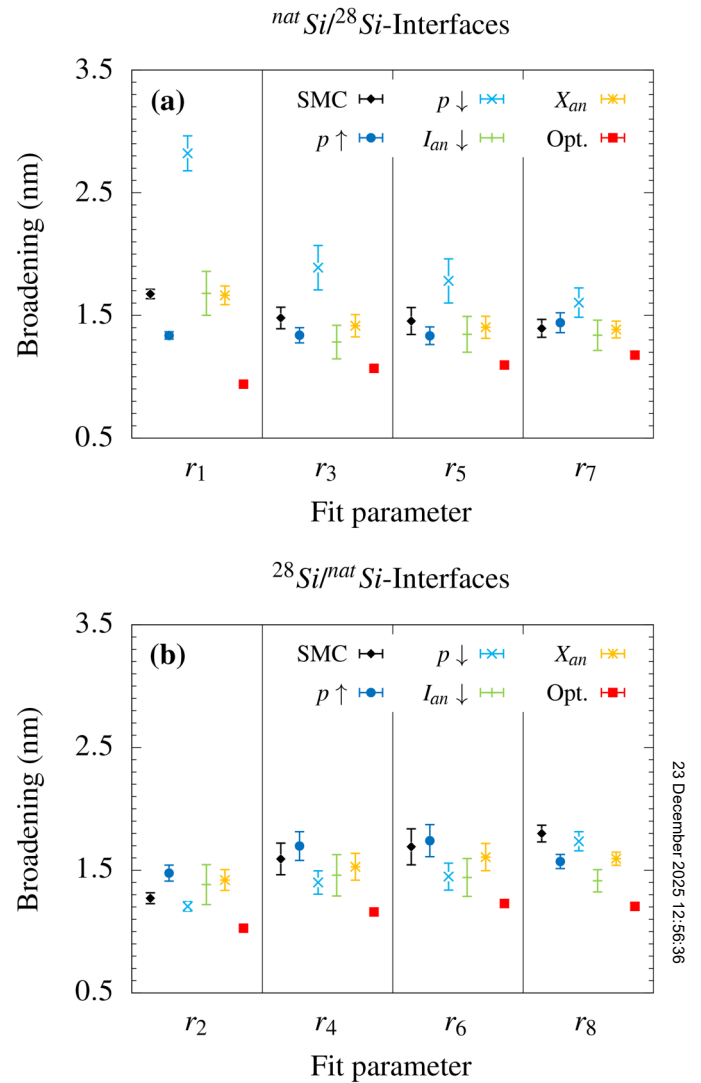
FIG. 7. Graphical presentation of the parameters r_i that describe the broadening of the interfaces, determined by fitting Eq. (1) to the experimental profiles of the test structure. (a) Broadening of the $^{nat}Si/^{28}Si$ interfaces; (b) broadening of the $^{28}Si/^{nat}Si$ interfaces. The error bars indicate the uncertainty of the fit. For the filled squares, the error bars are the same size or smaller than the symbols.

broadening of the topmost Si/^{28}Si interfaces [Fig. 7(a)] was determined to be slightly smaller than the broadening of the bottom ^{28}Si/Si interfaces [Fig. 7(b)], i.e., the topmost Si/^{28}Si interfaces seem slightly sharper than the bottom ^{28}Si/Si interfaces. Note that the same symbols appear higher on the broadening scale in Fig. 7(a) than in Fig. 7(b). For all measurements performed using a sputtering energy of 500 eV, broadening of deeper Si/^{28}Si interfaces was determined to be constant within the uncertainty of the fit. However, the uppermost Si/^{28}Si interface (r_1) appears more broadened (e.g., crosses in Fig. 7), due to transient changes in the

sputtering and ionization yield, which occur before the sputtering equilibrium has been established. In the case of a lowered flood gas pressure ($p \downarrow$), even deeper interfaces are influenced by changing ionization yields, resulting in a strong broadening [note the decreasing trend of the crosses in Fig. 7(a)]. For the measurement performed using a sputtering energy of 250 eV (Opt.), the broadening increases slightly with depth [note the increasing trend of the filled squares in Figs. 7(a) and 7(b)]. In this case, the sputtering equilibrium is reached before the topmost Si layer has been completely sputtered.

The broadening of the ^{28}Si/Si interfaces [Fig. 7(b)] seems to be slightly increased with depth, using a sputtering energy of 500 eV as well as 250 eV. However, a sputtering energy of 250 eV generally leads to the smallest broadening, both for the Si/^{28}Si interfaces and for the ^{28}Si/Si interfaces [note that filled squares are the lowest in Fig. 7(a) and 7(b). The error bars indicate that reduced instrumental broadening correlates with higher fitting accuracy.

A summary of the average changes in the interfacial broadening is given in Table II. Reducing the partial pressure of the flood gas ($p \downarrow$) led to a significantly increased broadening of the Si/^{28}Si interfaces (33 %), resulting in an average increase in the broadening parameter r by about 12 %. Increasing the partial pressure ($p \uparrow$) or using cluster ions for analysis (X_{an}) had no significant impact, while reducing the primary ion current ($I_{an} \downarrow$) led to a slightly less broadened profile. The greatest impact has the sputtering energy: while sputtering with 250 eV (Opt.), every interface appears significantly steeper than under standard measuring conditions, resulting in an average reduction of the broadening parameter r by about 27 %. This improvement in broadening coupled with the high fitting accuracy confirms that the profile Opt. is, as expected, closest to the true profile of the test structure within the parameter space explored in this study.

The fit parameters x_i that describe the layer thickness of sample #1 are graphically shown in Fig. 8. In the case the primary ion current is reduced ($I_{an} \downarrow$), the primary ion species is changed (X_{an}) and the gas pressure of the flood gas is increased ($p \uparrow$), the ^{nat}Si layers were determined to be slightly thicker than the ^{28}Si layers [the respective symbols appear higher on the thickness scale in Fig. 8(a) than in 8(b)]. In the case the flood gas pressure is reduced ($p \downarrow$) and the sputtering energy is reduced ($E^{\star} \downarrow$), the ^{nat}Si layers were determined to be slightly smaller than the ^{28}Si layers [the respective symbols appear lower on the thickness scale in Fig. 8(a) than in 8(b)]. The error bars indicate the uncertainty in fitting the model function (1) to the data. Deviations between the broadening of the different profiles, e.g., the SMC profile and the optimized (Opt.) profile, result from the instrumental broadening, which is determined by the respective measurement conditions. This instrumental broadening also affects the accuracy of the fit: the greater the instrumental broadening, the greater the uncertainty of the fit and the lower the instrumental broadening, the lower the uncertainty of the fit. Thus, the profile Opt. revealed the most reliable layer thicknesses that deviate by less than 0.5 nm from the nominal thickness of 2 nm. However, the thickness values for both ^{nat}Si layers and ^{28}Si layers seem to increase with depth, indicating a trend in the actual thickness.
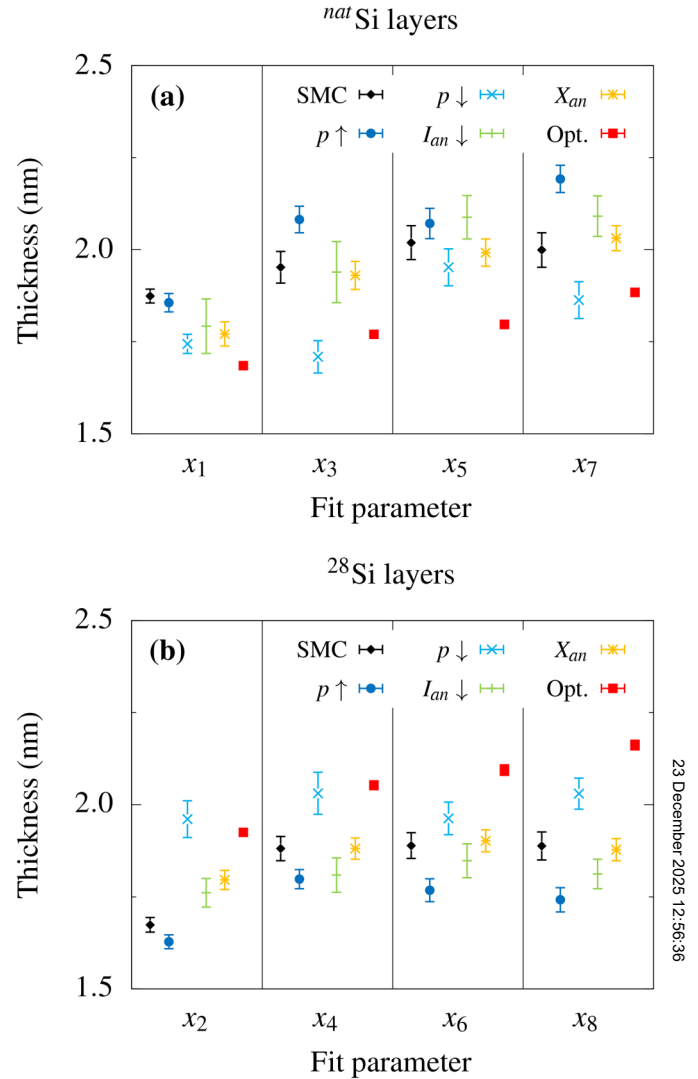
FIG. 8. Graphical presentation of the parameters x_i, that describe the thickness of the ^{nat}Si (x_i with $i = 1, 3, 5, 7$) and the ^{28}Si (x_i with $i = 2, 4, 6, 8$) layers, determined by fitting Eq. (1) to the experimental profiles of the test structure. The error bars indicate the uncertainty of the fit. For the filled squares, the error bars are the same size or smaller than the symbols.

6. Best sputter and analysis conditions

The profile Opt. [Fig. 6(b)] can be assumed to be closest to the true profile of sample #1 within the conditions tested in this study as the instrumental broadening is lowest. However, the filled squares in Figs. 7(a) and 7(b) show a slight increase in broadening with depth. Topography analysis by means of AFM indicates that this might be caused by a slight roughening of the sample surface during sputtering. The root-mean-square roughness was determined to be (0.4±0.1) nm on the initial surface and (0.6±0.1) nm in the ToF-SIMS crater.

Also note that the angle of incidence has a significant influence on the achievable depth resolution.[25] As with most SIMS instruments, the angle of incidence for the ToF-SIMS 5 instrument is fixed and we have not performed an angle variation study. Also note that for rough surfaces the angle of incidence is defined only very locally (depending on the respective angle of the surface) and cannot be controlled. Thus, the varying angle of incidence leads to a local variation in sputtering yield and can change the topography during sputtering. In order to evaluate the profile in terms of depth resolution, monitoring the topography, e.g., through AFM analysis before and after sputtering, can be helpful.

B. Depth profiling of a quantum well heterostructure

In contrast to the SIMS analysis of homostructures such as the isotopically modulated Si sample #1, the analysis of semiconductor heterostructures can be affected by the topography of the sample. This, in particular, becomes relevant for semiconductor layer structures with lattice parameters that differ from layer to layer. This lattice mismatch causes internal strain during epitaxial growth that can be relax by the formation of dislocations. These misfit dislocations result in corrugated surfaces with a roughness of several nanometers.[46] Prior to SIMS analysis, the topography of sample #2 was investigated by means of AFM. Figure 9(a) shows the topography of a $8 \times 8 \, \mu m^2$ reference area on the initial surface. The regularly wavy structure of the surface indicates surface corrugation. The root-mean-square roughness was determined to be (3.2 ± 0.1) nm. Therefore, ultimate lowered sputter energy at the expense of measurement time is not suitable in this case because the surface roughness limits the depth resolution. Taking the insights from the parameter variation study on sample #1 into account, the instrumental setup used for reference purposes was chosen for the depth profile analysis of sample #2. These settings provide sufficient depth resolution in view of the surface roughness and, in case SIMS analyses are performed commercially, the measurement time reduced by at least a factor of 10 due to the higher sputter energy limiting the costs for the analysis.

Figure 10 shows the measured concentration-depth profiles of ^{28}Si, ^{29}Si, and ^{74}Ge in the quantum well region. In general, the structure is well resolved. The thickness of the quantum well was determined to be (10.5 ± 0.2) nm, which corresponds to STEM data for this sample.[20]

Previous studies, e.g., by Drozdov et al.[47] (see also references therein), revealed the Ge/Si secondary ion intensity ratio measured from a $Si_{1-x}Ge_x$ layer to be related to the atomic fraction ratio by a constant factor for a wide range of Ge contents ($0.15 \leq x \leq 0.65$ for low-energy O_2^+ ion sputtering[48]). Dowsett et al.[49] mentioned that the Ge fraction x can be deduced directly as the ratio of Si^+ ion yield from the sample and bulk Si (e.g., from a Si wafer). The latter approach revealed the expected Ge content of 0.3 ± 0.02 for the top and bottom $Si_{0.7}Ge_{0.3}$ layer. As both, the ^{29}Si signal and ^{74}Ge signal, do not reach a plateau in the middle of the quantum well, the respective concentrations are expected to be high in this region. The residual concentration of ^{29}Si in the MBE source material is 41 ppm (0.0041 at %) according to the supplier, which is
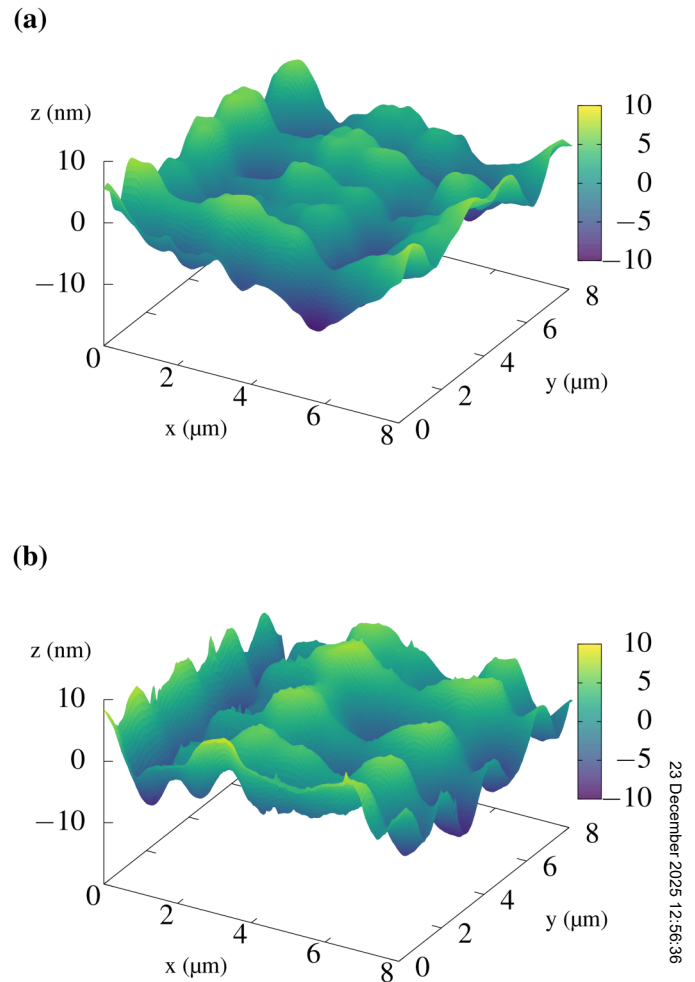
FIG. 9. Topography of a $8 \times 8 \, \mu m^2$ area on the initial surface (a) and in the crater (b) resulting from the ToF-SIMS analysis of sample #2 analyzed by means of atomic force microscopy. Surface corrugation resulting from strain relaxation via dislocations manifests in regular waves in two perpendicular crystal directions.

confirmed by means of APT analysis of the quantum well structure that yields a ^{29}Si concentration of (50 ± 20) ppm [(0.005 ± 0.002) at %] in the ^{28}Si quantum well.[20] For Ge, the APT measurement yields a concentration of 0.3 at % in the quantum well.[20] Assuming constant sputter and ionization yields through the whole structure, the ^{29}Si concentration was determined to $(2.5 \pm 0.1) \times 10^{19} \, cm^{-3}$ [(500.0 ± 0.2) ppm] and the ^{74}Ge to $(2.7 \pm 0.1) \times 10^{20} \, cm^{-3}$ in the ^{28}Si quantum well (fit parameter C_2). Taking the isotopic abundance of Ge into account, the residual Ge concentration within the ^{28}Si layer was calculated to $7.4 \times 10^{20} \, cm^{-3}$ (1.5 at %). Obviously, the ^{29}Si concentration as well as the Ge concentration in the quantum well are overestimated by means of ToF-SIMS. This is probably due to a lack of depth resolution caused by the roughness.
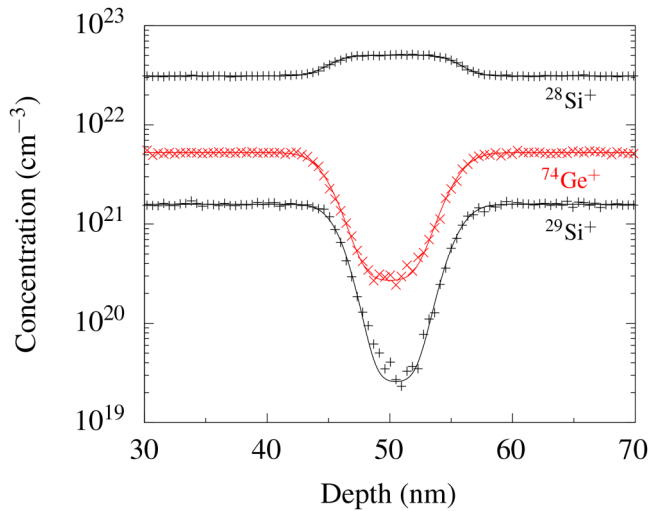
FIG. 10. SIMS concentration-depth profiles of ^{28}Si, ^{29}Si, and ^{74}Ge in the quantum well region of the $Si_{0.7}Ge_{0.3}/^{28}Si/Si_{0.7}Ge_{0.3}$ heterostructure. Measurement conditions: O_2^+, 500 eV, 40 nA, $300 \times 300\,\mu m^2$ sputtering; Bi_1^+, 15 keV, 0.25 pA, $75 \times 75\,\mu m^2$ analysis; O_2, 1×10^{-6} mbar flooding. Plus signs mark Si data and crosses mark Ge data. Every 10th data point is shown for clarity. The solid lines represent best fits based on Eq. (2) taking sputter broadening effects into account.

The fit parameters r_i that describe the interfacial broadening, determined by fitting Eq. (2) to the ^{28}Si data, the ^{29}Si data, and the Ge data, respectively, are summarized in Table III. The broadening at the top interface ($Si_{0.7}Ge_{0.3}/^{28}Si$) equals the broadening at the bottom interface ($^{28}Si/Si_{0.7}Ge_{0.3}$) within the uncertainty of the fit. However, the Ge profile tends to show a higher broadening than the ^{28}Si profile. Additionally, the ^{74}Ge signal starts to drop at a slightly lower sputtering depth than the ^{29}Si signal. This likely indicates a surface that is preferably terminated with Ge during growth,[43] which may be facilitated due to stronger Si–Si bonds compared to Si–Ge bonds.[38]

To ensure that sputtering has not induced additional roughness, the topography analysis by means of AFM was repeated in the crater. As shown in Fig. 9(b), surface corrugation can be observed manifesting in regular waves on a µm lateral scale in two perpendicular crystal directions. The root-mean-square roughness was determined to be $(3.2 \pm 0.1)\,nm$. This is the same value as

TABLE III. Fit parameters r_i that describe the interfacial broadening at the top interface ($i = 1$) and at the bottom interface ($i = 2$) of the quantum well heterostructure, determined by fitting Eq. (2) to the ^{28}Si data, ^{29}Si data, and the ^{74}Ge data, respectively.

	r_1 (nm)	r_2 (nm)
^{28}Si	1.9 ± 0.1	1.8 ± 0.1
^{29}Si	1.8 ± 0.1	1.9 ± 0.1
^{74}Ge	2.1 ± 0.1	2.2 ± 0.1

determined for the reference position on the initial surface, i.e., sputtering has not changed the surface roughness.

IV. CONCLUSION

ToF-SIMS has proven to be a suitable characterization method to determine isotopic concentration-depth profiles of semiconductor heterostructures. It has been shown that instruments used for routine analysis can also achieve a depth resolution below 1 nm, as long as the topography of the analyzed samples does not limit the depth resolution itself. When analyzing a test homostructure consisting of ultra-thin ^{nat}Si/^{28}Si bilayers of only 2 nm in thickness, the instrumental setting was optimized in favor of depth resolution, whereby, as expected, sputtering energy turned out to be the dominating parameter. It has been demonstrated that the consideration of the sputter rate ratio, i.e., the amount of material sputtered by both, the sputter beam and the analysis beam, plays a crucial role. In comparison to an instrumental setting used for routine analysis, the profile broadening was reduced by 27 % at the expense of measurement time, which was extended by the factor 14 in this study. Based on the results of this study, it is conceivable that a further reduction in sputtering energy could lead to a further reduction in instrumental broadening. However, 250 eV (Opt.) was the lowest possible sputtering energy that could be achieved with the device used, limited by the electronics that control the high voltage of the sputtering ion beam. It was shown that the insights from the variation study could be used to successfully resolve a SiGe/Si/SiGe heterostructure with a surface corrugation of several nm caused by the lattice mismatch between SiGe and Si. The thickness of the quantum well layer of this structure was determined to be (10.5 ± 0.2) nm in correspondence to STEM data.

Although the measurement conditions used in this work cannot be easily transferred to other interesting sample systems such as oxide heterostructures, AlN, GaN, and many others, the insights of the variation study can be helpful in finding the best measurement conditions for the individual sample system.

AUTHOR DECLARATIONS
Conflict of Interest

The authors have no conflicts to disclose.

Author Contributions

Jan Tröger: Formal analysis (lead); Writing – original draft (lead). **Reinhard Kersting:** Validation (supporting); Writing – review & editing (supporting). **Birgit Hagenhoff:** Resources (equal); Supervision (supporting); Writing – review & editing (equal).

23 December 2025 12:56:36

DATA AVAILABILITY

The data that support the findings of this study are available from the corresponding author upon reasonable request.

REFERENCES

[1] Z. I. Alferov, Rev. Mod. Phys. **73**, 767 (2001).

[2] H. Kroemer, Rev. Mod. Phys. **73**, 783 (2001).

[3] J. S. C. Kilby, ChemPhysChem **2**, 482 (2001).

[4] S. Nakamura, Rev. Mod. Phys. **87**, 1139 (2015).

[5] R. Xue, M. Beer, I. Seidler, S. Humpohl, J.-S. Tu, S. Trellenkamp, T. Struck, H. Bluhm, and L. R. Schreiber, Nat. Commun. **15**, 2296 (2024).

[6] G. Burkard, T. D. Ladd, A. Pan, J. M. Nichol, and J. R. Petta, Rev. Mod. Phys. **95**, 025003 (2023).

[7] A. Noiri, K. Takeda, T. Nakajima, T. Kobayashi, A. Sammak, G. Scapucci, and S. Tarucha, Nature **601**, 338 (2022).

[8] S. G. J. Philips, M. T. Madzik, S. V. Amitonov, S. L. de Snoo, M. Russ, N. Kalhor, C. Volk, W. I. L. Lawrie, D. Brousse, B. P. Tryputen, L. Wuetz, A. Sammak, M. Veldhorst, and G. Scappucci, Nature **609**, 919 (2022).

[9] X. Xue, M. Russ, N. Samkharadze, B. Undseth, A. Sammak, G. Scappucci, and L. M. K. Vandersypen, Nature **601**, 343 (2022).

[10] W. Huang, C. H. Yang, K. W. Chan, T. Tanttu, B. Hensen, R. C. C. Leon, M. A. Fogarty, J. C. C. Hwang, F. E. Hudson, K. M. Itoh, A. Morello, A. Laucht, and A. S. Dzurak, Nature **569**, 532 (2019).

[11] N. W. Hendrickx, W. I. L. Lawrie, M. Russ, F. van Riggelen, S. L. de Snoo, R. N. Schouten, A. Sammak, G. Scappucci, and M. Veldhorst, Nature **591**, 580 (2021).

[12] G. Scappucci, C. Kloeffel, F. A. Zwanenburg, D. Loss, M. Myronov, J.-J. Zhang, S. de Franceschi, G. Katsaros, and M. Veldhorst, Nat. Rev. Mater. **6**, 926 (2021).

[13] H. Bluhm and L. R. Schreiber, in *2019 IEEE International Symposium on Circuits and Systems (ISCAS)* (IEEE, 2019), pp. 1–5.

[14] J. Yoneda, K. Takeda, T. Otsuka, T. Nakajima, M. R. Delbecq, G. Allison, T. Honda, T. Kodera, S. Oda, Y. Hoshi, N. Usami, K. M. Itoh, and S. Tarucha, Nat. Nanotechnol. **13**, 102 (2018).

[15] F. A. Zwanenburg, A. S. Dzurak, A. Morello, M. Y. Simmons, L. C. L. Hollenberg, G. Klimeck, S. Rogge, S. N. Coppersmith, and M. A. Eriksson, Rev. Mod. Phys. **85**, 961 (2013).

[16] A. Wild, J. Kierig, J. Sailer, J. W. Ager, E. Haller, G. Abstreiter, S. Ludwig, and D. Bougeard, Appl. Phys. Lett. **100**, 143110 (2012).

[17] V. Jmerik, Nanomaterials **12**, 1 (2022).

[18] M. P. Losert, M. A. Eriksson, R. Joynt, R. Rahman, G. Scappucci, S. N. Coppersmith, and M. Friesen, Phys. Rev. B **108**, 125405 (2023).

[19] M. Volmer, T. Struck, A. Sala, B. Chen, M. Oberländer, T. Offermann, R. Xue, L. Visser, J.-S. Tu, S. Trellenkamp, Ł. Cywiński, H. Bluhm, and L. R. Schreiber, npj Quantum Inf. **10**, 61 (2024).

[20] J. Klos, J. Tröger, J. Keutgen, M. P. Losert, H. Riemann, N. V. Abrosimov, J. Knoch, H. Bracht, S. N. Coppersmith, M. Friesen, O. Cojocaru-Mirédin, L. R. Schreiber, and D. Bougeard, "Atomistic compositional details and their importance for spin qubits in isotope-purified silicon quantum wells," Adv. Sci. **11**(42), 2407442 (2024).

[21] M. Neul, I. V. Sprave, L. K. Diebel, L. G. Zinkl, F. Fuchs, Y. Yamamoto, C. Vedder, D. Bougeard, and L. R. Schreiber, Phys. Rev. Mater. **8**, 043801 (2024).

[22] G. Servanton, R. Pantel, M. Juhel, and F. Bertin, Micron **40**, 543 (2009).

[23] B. Gault, A. Chiaramonti, O. Cojocaru-Mirédin, P. Stender, R. Dubosq, C. Freysoldt, S. K. Makineni, T. Li, M. Moody, and J. M. Cairney, Nat. Rev. Methods Primers **1**, 51 (2021).

[24] R. Möllers and E. Niehuis, "Secondary ion mass spectrometer and secondary ion mass spectrometric method," U.S. patent 10,354,851 (16 July 2019).

[25] S. Hofmann, Rep. Prog. Phys. **61**, 827 (1998).

[26] S. Hofmann, "Ultimate depth resolution and profile reconstruction in sputter profiling with AES and SIMS," Surf. interface anal. **30**(1), 228–236 (2000).

[27] Y. Yamamura, Nucl. Instrum. Methods Phys. Res. **194**, 515 (1982).

[28] Y. Yamamura, Nucl. Instrum. Methods Phys. Res., Sect. B **33**, 493 (1988).

[29] F. Jahnel and R. Criegern, Appl. Surf. Sci. **203–204**, 367 (2003).

[30] T. Grehl, R. Möllers, and E. Niehuis, Appl. Surf. Sci. **203–204**, 277 (2003).

[31] R. Liu and A. Wee, Appl. Surf. Sci. **231–232**, 653 (2004).

[32] T. Struck, A. Hollmann, F. Schauer, O. Fedorets, A. Schmidbauer, K. Sawano, H. Riemann, N. V. Abrosimov, Ł. Cywiński, D. Bougeard, and L. R. Schreiber, npj Quantum Inf. **6**, 40 (2020).

[33] T. Struck, M. Volmer, L. Visser, T. Offermann, R. Xue, J.-S. Tu, S. Trellenkamp, Ł. Cywiński, H. Bluhm, and L. R. Schreiber, Nat. Commun. **15**, 1325 (2024).

[34] K. Iltgen, C. Bendel, A. Benninghoven, and E. Niehuis, "Optimized time-of-flight secondary ion mass spectroscopy depth profiling with a dual beam technique," J. Vac. Sci. Technol. A **15**(3), 460–464 (1997).

[35] K. Elst, W. Vandervorst, J. Alay, J. Snauwaert, and L. Hellemans, "Influence of oxygen on the formation of ripples on Si," J. vac. sci. technol. B **11**(6), 1968–1981 (1993).

[36] N. Matsunami, Y. Yamamura, Y. Itikawa, N. Itoh, Y. Kazumata, S. Miyagawa, K. Morita, R. Shimizu, and H. Tawara, At. Data Nucl. Data Tables **31**, 1 (1984).

[37] C. M. Ng, A. T. S. Wee, C. H. A. Huan, and A. See, "Effects of oxygen flooding on crater bottom composition and roughness in ultrashallow secondary ion mass spectrometry depth profiling," J. vac. sci. technol. B, **19**(3), 829–835 (2001).

[38] D. R. Lide, *CRC Handbook of Chemistry and Physics*, 90th ed. (Taylor & Francis, 2009).

[39] B. Paquelet Wuetz, M. P. Losert, S. Koelling, L. E. Stehouwer, A.-M. J. Zwerver, S. G. Philips, M. T. Mkadzik, X. Xue, G. Zheng, M. Lodari *et al.*, Nat. Commun. **13**, 7730 (2022).

[40] O. Dyck, D. N. Leonard, L. F. Edge, C. A. Jackson, E. J. Pritchett, P. W. Deelman, and J. D. Poplawsky, Adv. Mater. Interfaces **4**, 1700622 (2017).

[41] T. Südkamp and H. Bracht, "Self-diffusion in crystalline silicon: A single diffusion activation enthalpy down to 755°C," Phys. Rev. B **94**(12), 125208 (2016).

[42] R. Kube, H. Bracht, E. Hüger, H. Schmidt, J. L. Hansen, A. N. Larsen, J. W. I. Ager, E. E. Haller, T. Geue, and J. Stahn, Phys. Rev. B **88**, 085206 (2013).

[43] R. Kube, H. Bracht, J. L. Hansen, A. N. Larsen, E. E. Haller, S. Paul, and W. Lerch, J. Appl. Phys. **107**, 073520 (2010).

[44] M. V. Medvedeva, I. A. Wojciechowski, and B. J. Garrison, Surf. Sci. **505**, 349 (2002).

[45] T. Grehl, *Improvement in TOF-SIMS Instrumentation for Analytical Application and Fundamental Research*, Electronic ed., edited by A. Benninghoven (University of Münster, 2003).

[46] E. Kasper and S. Heim, Appl. Surf. Sci. **224**, 3 (2004).

[47] M. N. Drozdov, Y. N. Drozdov, A. Csík, A. V. Novikov, K. Vad, P. A. Yunin, D. V. Yurasov, S. F. Belykh, G. P. Gololobov, D. V. Suvorov *et al.*, Thin Solid Films **607**, 25 (2016).

[48] Z. Jiang, K. Kim, J. Lerma, A. Corbett, D. D. Sieloff, M. L. Kottke, R. B. Gregory, and S. Schauer, Appl. Surf. Sci. **252**, 7262 (2006).

[49] M. G. Dowsett, R. J. Morris, P.-F. Chou, S. F. Corcoran, H. Kheyrandish, G. A. Cooke, J. L. Maul, and S. Patel, Appl. Surf. Sci. **203**, 500 (2003).

23 December 2025 12:56:36